Role of molecular damage in crack initiation mechanisms of tough elastomers

Jianzhu Ju, Gabriel Sanoja, Luca Cipelletti, Matteo Ciccotti, Bangguo Zhu, Tetsuharu Narita, Chung Yuen Hui, Costantino Creton

PNAS RESEARCH ARTICLE | APPLIED PHYSICAL SCIENCES

Role of molecular damage in crack initiation mechanisms of tough elastomers

Jianzhu Ju[a], Gabriel E. Sanoja[a,b], Luca Cipelletti[c,d], Matteo Ciccotti[a], Bangguo Zhu[e], Tetsuharu Narita[a], Chung Yuen Hui[e,1], and Costantino Creton[a,1]

Affiliations are included on p. 8.

Edited by Anna Balazs, University of Pittsburgh, Pittsburgh, PA; received May 26, 2024; accepted September 23, 2024

Tough soft materials such as multiple network elastomers (MNE) or filled elastomers are typically stretchable and include significant energy dissipation mechanisms that prevent or delay crack growth. Yet most studies and fracture models focus on steady-state propagation and damage is assumed to be decoupled from the local stress and strain fields near the crack tip. We report an in situ spatial-temporally resolved 3D measurement of molecular damage in mechanophore-labeled MNE just before a crack propagates. This technique, complemented by digital image correlation, allows us to compare the spatial distribution of both damage and deformation in single network (SN) elastomers and in MNE. Compared to SN, MNE have a wide-spread damage in front of the crack and, surprisingly, delocalize strain concentration. A continuum model, where damage distribution is fully coupled to the crack tip fields, is proposed to explain these results. Additional measurements of time-dependent molecular damage during fixed grips relaxation in the presence of a crack reveal that the less localized damage distribution delays fracture initiation. The observations and exploratory modeling reveal the dynamic fracture mechanism of MNE, providing guidance for rational design of high-performance tough elastomers.

elastomers | mechanochemistry | digital image correlation | damage | fracture

Significance

Tough elastomers can stretch reversibly to large deformations without breaking because of internal energy dissipation mechanisms that slow down crack growth. By combining a temporal and spatial quantification of broken chemical bonds, and a microscopic tool, to measure the strain field near a defect, we show that in tough elastomers the material may also mitigate strain concentrations by breaking selected chemical bonds, resulting in a homogeneization of strain and a delayed crack nucleation. By introducing a measure of the damage distribution singularity n, we propose an analytical model successfully describing the sharp increase in crack initiation strain between simple and tough elastomers.

Multiple network elastomers (MNE) are a class of recently developed soft materials inspired by double network hydrogels (1), and possessing an interesting combination of high stiffness, good reversible extensibility, and high toughness (2–5). Their excellent mechanical performance stems from the presence of the embedded sacrificial network, so that the material can be highly deformed and damaged while still resisting fracture (1, 2). The very high fracture energy, over 10^3 J/m^2, for a highly elastic material has been attributed to an energy dissipation mechanism by bond scission localized near the crack tip (2, 6). Engineering of tough hydrogels and elastomers by network design is becoming a new hot topic in polymer science (7–10), but the focus has mainly been on developing new materials. A consistent molecular picture of the large increase in fracture toughness in MNE (a very general effect) is still elusive. This molecular picture is crucial for precisely designing and controlling the toughness of MNE, and requires a comprehensive understanding of how molecular damage is related to the failure process.

The classical Lake and Thomas theory of fracture (11) assumes that dissipation by damage is highly localized near the crack tip: The broken chemical bonds are restricted to the dimensions of a network mesh size ~10 nm directly ahead of the crack tip, i.e. the fracture process zone. This assumption suggests that damage can be decoupled from the calculation of stress and strain fields, and that the fracture occurs instantly when the strain energy release rate $\mathcal{G}$ exceeds the fracture energy Γ (12). The implicit assumption is that rupture of molecular bonds corresponds to the increase of the crack length, while the material outside the process zone remains intact. However, this picture is not supported by the recently developed mechanophore-based optical techniques (2, 13–16), which show that in MNE the damaged region can be of millimeter scale (2, 3, 6) without causing any crack propagation. Such macroscopic damage may blunt the crack tip, reducing the stress and increasing the size of the region subjected to strain concentration. This region has been observed in experiments (17–21) and simulations (18, 22–25) and is typically of the order of 100 μm or more around the crack tip (12, 26, 27). MNE feature a strong coupling between damage and strain field and, while the existence of damage has been discussed and modeled (6, 22, 28, 29), a proper molecular failure criterion is still missing.

In this work, we present an in-depth description of the fracture behavior of MNE, emphasizing the coupling between damage distribution and strain fields near the crack

Author contributions: J.J., L.C., T.N., C.Y.H., and C.C. designed research; J.J., G.E.S., M.C., B.Z., and C.Y.H. performed research; G.E.S. contributed new reagents/analytic tools; J.J., L.C., M.C., B.Z., T.N., C.Y.H., and C.C. analyzed data; and J.J., G.E.S., L.C., M.C., B.Z., T.N., C.Y.H., and C.C. wrote the paper.

The authors declare no competing interest.

This article is a PNAS Direct Submission.

[1]To whom correspondence may be addressed. Email: ch45@cornell.edu or Costantino.Creton@espci.psl.eu.

This article contains supporting information online at https://www.pnas.org/lookup/suppl/doi:10.1073/pnas.2410515121/-/DCSupplemental.

Published October 30, 2024.

tip. The critical role played by the spatial and time dependence of molecular damage is studied using a model MNE, which is partially crosslinked with mechanophores. Full-scale dynamic information of damage and deformation during fracture is determined by combining simultaneous 3D damage visualization using confocal microscopy and digital image correlation (DIC). While indirect evidence of damage near the crack tip has been reported using other methods during/after propagation (2–4, 17), the experiments presented here provide 3D high resolution (2 μm/pixel in plane and 150 μm/slice in depth for the more prestretched MNE) mapping of bond scission near an open crack, *long before* propagation. When comparing with the behavior of single networks (SN), we found that the fracture strength of MNE is enhanced by the widespread distribution of damage that leads to a delocalization of the deformation field. Furthermore, MNE shows a high resistance against delayed fracture, accompanied by a time-dependent crack tip damage accumulation at fixed macroscopic deformation. A simple analytical model is proposed to explain the results, which explores the interplay between damage distribution and crack tip fields.

Spatial Distribution of Damage and Deformation

Mechanical testing and in situ observation of single-edge notched (SEN) samples subjected to uniaxial extension are simultaneously performed with mechanophore imaging by confocal microscopy (from the top of the sample) and DIC by a CMOS (complementary metal oxide semiconductor) camera (from the bottom of the sample), using the experimental set-up shown in Fig. 1*A*. The bottom face of the sample is spray painted to generate speckles for DIC analysis. Details are provided in *Materials and methods*. Following our previous work on poly (ethyl acrylate) (EA) multiple networks (3–5, 30), moderately prestretched double networks (DN) and highly prestretched triple networks (TN) were prepared by Ultraviolet (UV)-polymerization of the swollen SN, as seen in *Materials and methods*. The degree of prestretch, elastic modulus, and stretch at break are shown in Table 1. The SN is synthesized first with 5 mol% of the crosslinker labeled with the mechanophore (nonfluorescent in the intact state), and then swelled in an EA monomer solution and polymerized again, leading to isotropic prestretching of the first network (also called sacrificial or filler network). The difference in extensibility between filler network and second/third network (matrix network) results in the progressive breaking of bonds in the minority prestretched filler network during large deformation (3, 28). The degree of prestretch λ_0 of the filler network is related to the isotropic volume swelling ratio α by $\lambda_0 = \sqrt[3]{\alpha}$ (Table 1).

SEN samples of SN and MNE are continuously and uniaxially stretched until fracture with a stretch rate $\dot{\lambda} = 10^{-4}\ s^{-1}$. To avoid different crack profiles at different depths from the surface, a modified cutting method is applied (*Materials and Methods*), with crack length around 1.5 mm for all samples. The stress-stretch curves are shown in Fig. 1*B*. As previously reported (2, 5, 20), a significant increase in modulus and stretch at break/crack propagation is observed in the notched samples of MNE relative to those of SN (also summarized in Table 1). During the propagation of the

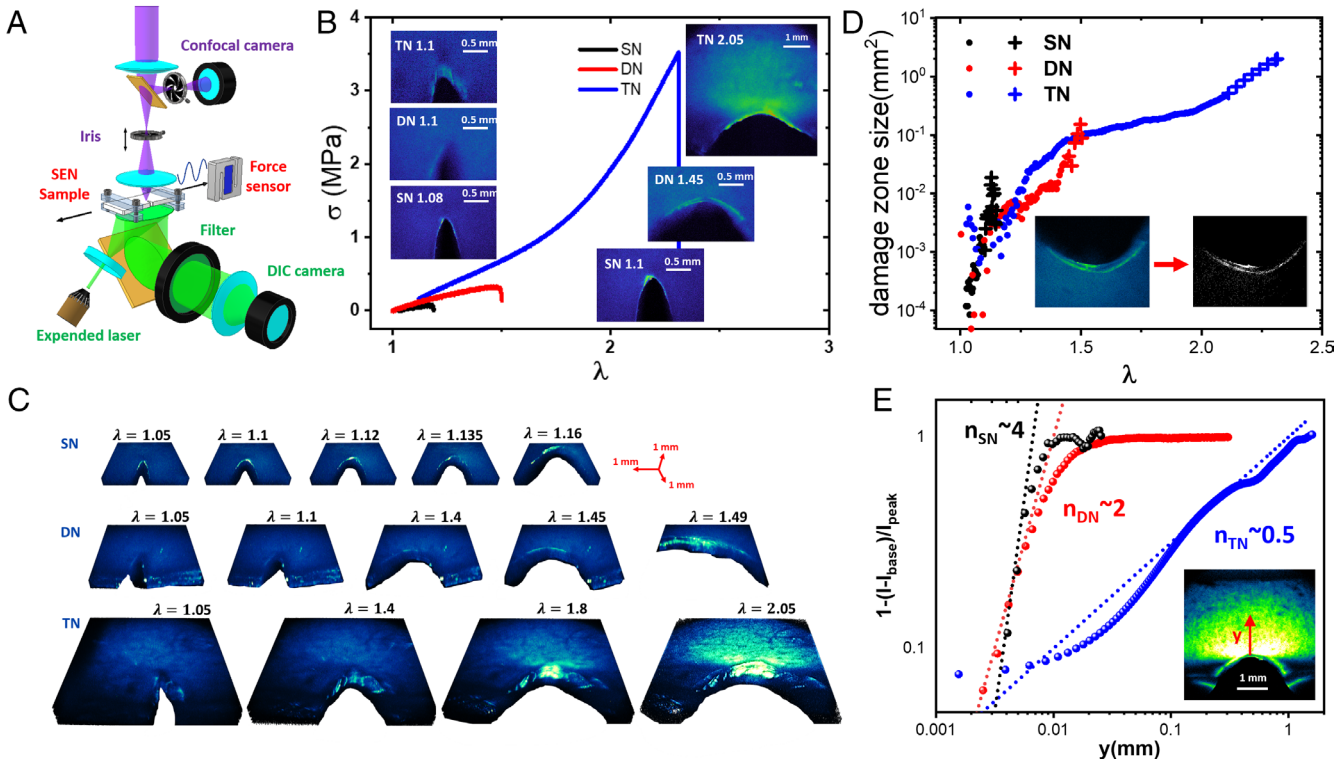

Fig. 1. (*A*) Schematic of the set-up for the simultaneous measurement of the strain field near the crack tip by DIC and of the molecular damage map by mechanophore activation. (*B*) Stress-stretch curve during uniaxial extension of notched SN, DN, and TN respectively, with a stretch rate = $10^{-4}\ s^{-1}$. SEN samples of SN, DN, and TN are cut into samples with the same lateral dimensions for fracture testing: 15 mm length (between clamps) × 6 mm width. *Inset*: 2D fluorescence intensity distribution around the crack tip for SN, DN, and TN, at small stretch (*Left*) and just before propagation (*Right*). (*C*) 3D damage maps of fluorescence intensity by confocal microscopy, in SN, DN, and TN at different values of λ. (*D*) The size of the damage zone for SN, DN, and TN as a function of λ. At large λ, a slight crack propagation can already be observed during stretching. Results before propagation are indicated by "●," and those after are indicated by "+." *Inset*: an example showing the extracted damage zone area from 2D fluorescence images, where mechanophore mapping is converted to binary images with the defined threshold. (*E*) Fluorescence intensity as a function of the distance away from the crack tip y for different materials right before propagation. *Inset*: the coordinate based on crack tip position. λ in the images are 1.1, 1.45, and 2 for SN, DN, and TN, respectively.

Table 1. Sample specifications and mechanical properties of SN, DN, and TN

	SN	DN	TN
Prestretch λ_0	1	1.59	2.34
Thickness	0.8 mm	1.27 mm	1.83 mm
Young modulus E	0.47 MPa	0.96 MPa	1.36 MPa
λ at break	1.19	1.5	2.31
λ of crack propagation onset	1.1	1.45	2.1

crack, a much faster propagation speed (at the same stretch rate of $\dot{\lambda} = 10^{-4}$ s^{-1}) is found in MNE compared to SN, as seen in *SI Appendix*, Fig. S1. Before propagation, the crack gradually opens with increasing λ, and mechanophore crosslinkers irreversibly activate by force-induced chemical reaction and bond breaking. Details on the chemistry of these crosslinkers can be found in Göstl and Sijbesma (14) or Slootman et al. (16). In our data acquisition, spatially resolved fluorescence intensity (due to breaking of mechanophore crosslinkers) is acquired with a time resolution of 1 min by confocal microscopy to achieve a depth-resolved map (4, 31, 32). Images of fluorescence intensity at a depth where the most damage is observed are shown in Fig. 1*B*, at small $\lambda \sim 1.1$ and right before crack propagation. Right before crack propagation, TN has a significantly larger damage zone than DN and SN, consistent with the observations previously made with other mechanophores like dioxetane (3). Note that because the primary purpose of the experiment is to follow the time dependence of the activation, the fluorescence is not calibrated in absolute terms against a sample with a known concentration of fluorescent molecules as in some of our previous studies (3, 4, 16).

Fig. 1*C* shows 3D damage maps for three different networks at different λ. In TN, even though crack propagation occurs at $\lambda = 2.1$, massive damage far from the crack tip (~1 mm) is observed at $\lambda = 1.8$. The spatial distribution of damage at large stretch ($\lambda = 1.8$ and $\lambda = 2.05$ in Fig. 1*C*) in TN shows a growing pattern similar to the region of strain concentration around the crack, previously observed during crack blunting in similar soft elastic materials by DIC and by simulations (18, 33). A slice of the damage zone (observed at a depth where the most damage is observed) is shown in the inset of Fig. 1*D*. The activated area of that slice (in mm^2) is calculated as a function of time for each sample relative to a threshold representative of the background intensity. As the damage levels are significantly different in SN, DN, and TN, the quantification of the damaged area is strongly influenced by the data noise level (especially in SN). To better capture the damaged area, the thresholds are subjectively adjusted for each sample to capture the activated area due to damage (inset of Fig. 1*D*). Significant growth of the damage zone before propagation can be quantified for MNE, reaching a much larger scale (~0.05 mm^2 in DN and 0.5 mm^2 in TN) than SN, which is strikingly 10^9 and 10^{10} times larger than the prediction of the Lake-Thomas theory (11) (in terms of area).

To quantitatively compare the extent of the damage distribution, the y-dependent (along the propagation direction) fluorescence intensities right before crack propagation in each material are extracted (averaged over a width along the x direction of 0.1 mm) and plotted in Fig. 1*E*. These images with a better spatial/intensity resolution are collected here in static conditions (gradually increasing the stretch and then fixed λ for a long collection time). λ in the images are 1.1, 1.45, and 2 for SN, DN, and TN, respectively. In Fig. 1*E*, we plot $1 - ((I - I_{base})/I_{peak})$ where I_{base} is the intensity far from the crack tip and I_{peak} is the value of intensity as close to the crack tip as our spatial resolution (~1 μm) allows. This representation of the data shows that a more delocalized distribution of damage can be seen in TN, with an exponent $n_{TN} \sim 0.5$ in log–log scale, (comparing with SN and DN where $n_{SN} \sim 4$ and $n_{DN} \sim 2$ respectively), spreading over a size over 1 mm. The scaling of the damage distribution will be further discussed later.

We now turn to DIC to determine the strain field ahead of the crack tip. To better visualize the strain localization and avoid the cumulative errors during large strain calculation, the L_{xx} component of the velocity gradient tensor $\boldsymbol{L}$ in the deformed configuration is plotted as a 2D map in Fig. 2*A* (*Materials and Methods* for details). Surprisingly, by comparing the L_{xx} maps of the three elastomers, we find that the MNE homogenize the strain rate: At the same λ, a much larger L_{xx} is observed around the crack tip in SN than in DN and TN. We determined the Hencky strain tensor $\boldsymbol{\varepsilon}$ in the undeformed coordinates by DIC, and the component in the stretching direction (ε_{xx}) is shown in Fig. 2*B* as a function of y, the distance from the crack tip in the undeformed coordinates along the symmetric line. Note that in uniaxial tension the Hencky strain is defined as $ln\lambda$. At the same macroscopic λ, a smaller ε_{xx} can be detected in TN than in DN and SN. ε_{xx} at $y = 0.3$ mm for the three materials are extracted from $\varepsilon_{xx}(y)$ and shown in Fig. 2*C* as a function of λ, as long as crack extension is less than $y = 0.3$ mm. For $\lambda < 1.05$, ε_{xx} nearly overlaps for all three materials, while an obvious increase in ε_{xx} is detected at $\lambda \sim 1.05$ for SN and at $\lambda \sim 1.15$ for DN. When comparing ε_{xx} and the damage area of DN and TN (Fig. 2*D*), it can be found that from the value of applied stretch λ where a significant damage is observed in TN ($\lambda > 1.2$), the strain field in the TN ahead of the crack grows less with λ relative to the DN. In summary, the multiple network architecture combines extensive damage and a very low level of strain concentration ahead of the crack tip.

While the results reported here have been obtained for a particular type of DN and TN based on poly(EA) our results suggest that the transition between continuous crack growth (observed in SN) and full spatial distribution of damage in the bulk (observed in the TN), should be rather general and continuous with increasing degree of prestretch λ_0 and increasing dilution of the filler network. Yet it is very likely that details may differ and be dependent of the degree of crosslinking of the filler network and the degree of mechanical coupling between the networks. Further systematic experiments as a function of λ_0 would be needed to unveil these differences.

An MNE Model: Coupling Damage and Strain Distributions

Simultaneous mapping of damage and deformation, together with the clear enhancement of the fracture resistance, show that a large damage zone in the MNE is accompanied by strain *delocalization* around the crack tip (in comparison with SN). This seems counterintuitive: A more damaged region should be somehow more deformed. Remarkably, in the MNE, molecular damage takes place over a macroscopic scale (around 5 mm in Fig. 1*B*) as observed by confocal microscopy, while the classical fracture theory assumes that local damage does not affect the stress and strain distributions (12, 34). Given the large size of the damage zone, the coupling of damage and deformation is expected to influence the fracture process cooperatively. To address this challenging problem, we propose a model including progressive damage into the analysis of crack tip fields. In order to avoid complications due to crack opening in mode I, we consider a Mode III crack in a neo-Hookean solid (35). In SN,

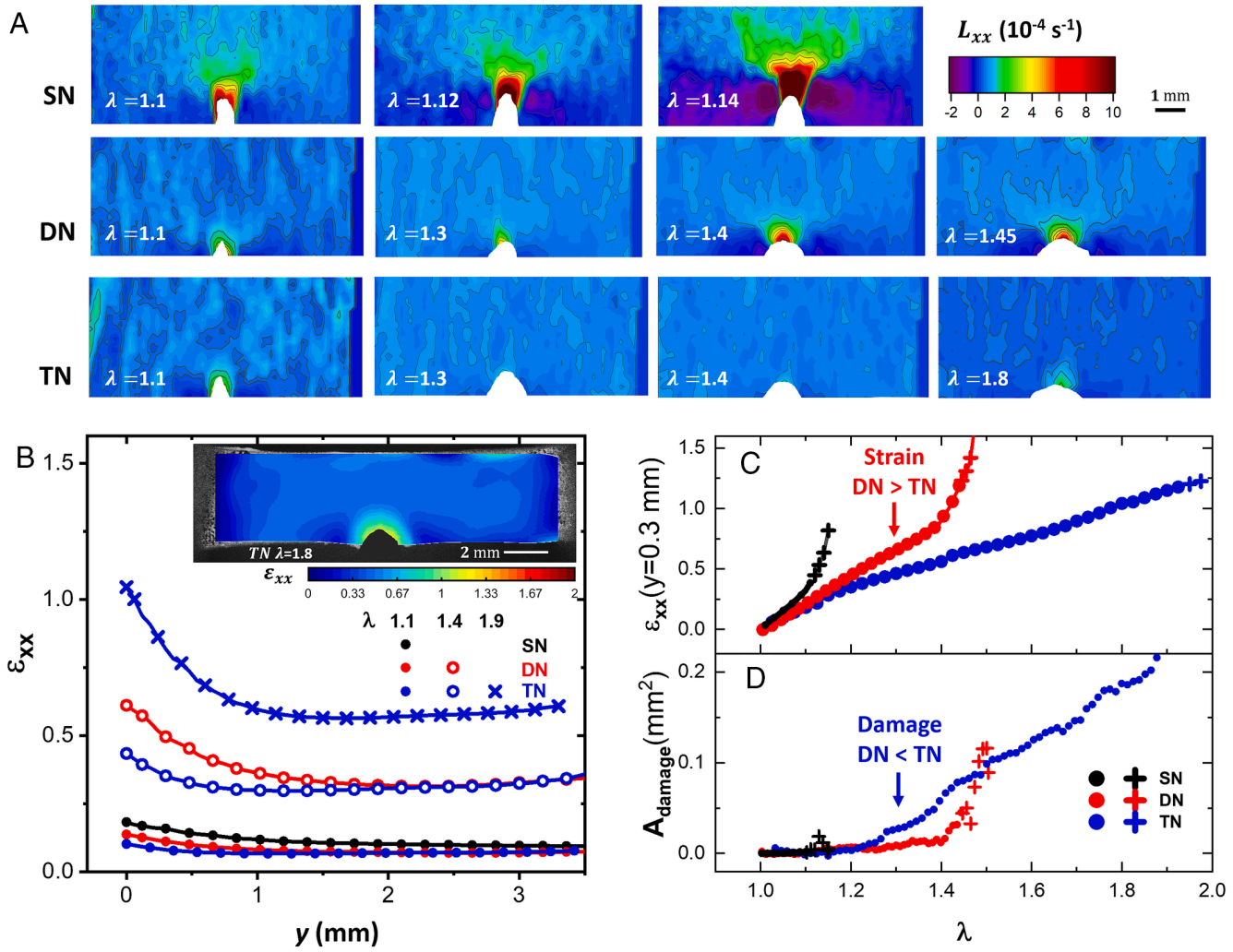

Fig. 2. (*A*) Strain rate map for SN, DN, and TN at different values of macroscopic λ. (*B*) Hencky strain ε_{xx} as a function of y at λ = 1.1, 1.4, and 1.9, respectively. y is the vertical distance from the crack tip in the undeformed configuration. The results are averaged over a width along the x direction of 0.45 mm. *Inset*: ε_{xx} map of TN at λ = 1.8, shown in deformed configuration for better visualization. (*C*) ε_{xx} at y = 0.3 mm from the crack tip as function of λ. At large λ, slight propagation (total propagation is below 0.3 mm in all shown results) can already be observed during stretching. Results before propagation are indicated by ●, and those after are indicated by +. (*D*) The area of the damage zone (same data as Fig. 1*D* but plotted in linear scale) as the function of λ.

damage is due to chain scission in the network, and the modulus of the elastomers is proportional to the density of chains. However, in MNE the damage occurs predominantly in the filler network (the first being synthesized) and the modulus decreases with chain scission following two separate regimes: At moderate strains, the modulus is nearly unaffected by chain scission (2, 5), while above a critical strain where a yielding process occurs, the modulus decreases markedly (5). In our model, we use the shear modulus to characterize damage in both materials. As seen in Fig. 3*A*, the damage zone in a polar coordinate (r, θ) is defined by a circle with radius ρ, and the distribution of damage is represented by an r-dependent shear modulus G:

$$G(r) = G_0(r/\rho)^n \qquad r < \rho,$$

$$G(r) = G_0 \qquad r > \rho, \qquad [1]$$

G_0 is the modulus of the undamaged solid, and $n > 0$ is the key parameter controlling damage distribution. For example, one expects $n \gg 1$ for SN, and $n \sim O(1)$ for MNE, as suggested by Fig. 1*E*. This is because the breakage of the sacrificial (filler) network far from the tip has only a small effect on the modulus in MNE due to the existence of the less deformed matrix network and only very close to the tip does the damage cause a significant decrease in modulus due to yielding. For the SN all bonds contribute to decreasing the modulus and most of the bonds are broken inside a small zone (damage is highly localized) (5, 28). Note that Fig. 3*B* shows G/G_0 as a function of a normalized length. The absolute radius of the gray zone ($r = \rho$) will be very different in SN and TN as shown in Fig. 1*E*.

The evolution of the modulus due to damage for different values of n is schematically described in Fig. 3*B*. ρ is a parameter in the model, which is related to the external load and load transfer mechanism. Unlike the classical fracture mechanics formalism where the damage is neglected in the stress and strain field calculation (small-scale yielding approximation), we assume here that the fracture takes place when the modulus (due to damage) decreases to a certain level, G_f, at some fixed material distance $r = d$ directly ahead of the crack tip. The distance d is introduced since our damage model has no intrinsic length scale and the description of fracture requires a microscopic length scale.

Using Eq. **1** this condition is

$$G_f = G(r=d) = G_0\left(d/\rho_f\right)^n, \qquad [2]$$

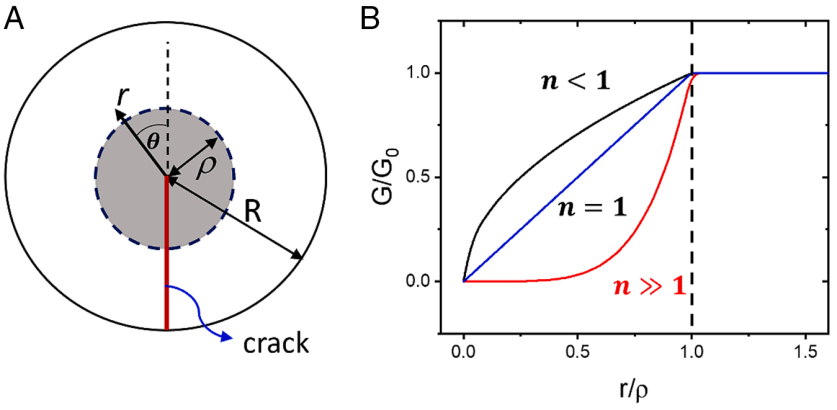

Fig. 3. (*A*) Schematic of a damage zone (gray) with radius of ρ around the crack. r and θ give the polar coordinate and displacement is prescribed on the outer circle $r = R$. (*B*) Damage (represented by modulus G/G_0) distribution with different mode n.

where $\rho_f = \left(G_0/G_f\right)^{1/n} d$ is the size of the damage zone at fracture. We expect $G_0/G_f \gg 1$, so that a substantial decrease in local modulus (and a substantial molecular damage) is required for fracture. For SN, *n is large*, so the condition $G_0/G_f \gg 1$ is easily satisfied by $\rho_f \approx O(d)$. This means that the size of the damage zone is small and nearly the same as the distance at which the modulus is equal to G_f.

However, for small n (MNE), we need $\rho_f \gg d$ to satisfy this condition; hence ρ_f can be macroscopic, as observed in Fig. 1. During a continuous deformation around a crack, as ρ is initially 0 (before deformation), for $G_0(d/\rho)^n$ to decrease to G_f, ρ must increase to ρ_f, i.e., the damage zone should grow before fracture occurs.

This growth of the damage zone before fracture arises, is observed in our experiments and was observed also in recent experiments of crack propagation in double network gels (36). These experiments suggest that the distance d where the filler network is significantly damaged (~50 μm in the observations of refs. 20 and 30) could be related to the point where the matrix networks become loaded and the filler network is extensively broken (30, 37). This remains however a hypothesis since the local variation of the modulus in the damage zone remains unknown. Further discussion is included in *Supplementary information* 2.3.

We test the model by loading a crack with a prescribed displacement on the outer circle $r = R$ in Fig. 3*A*, i.e., $w(r = R, \theta) = W_0 \sin(\theta/2)$, where W_0 represents the intensity of the applied displacement. The strain fields in the damage regions are (details are shown in *Supporting information*):

$$\gamma_\theta(r < \rho, \theta) = \frac{Ar^{\eta-1}}{2} cos(\theta/2), \qquad [3]$$

$$\gamma_r(r < \rho, \theta) = A\eta r^{\eta-1} \sin(\theta/2), \qquad [4]$$

where $\eta = \frac{-n+\sqrt{1+n^2}}{2}$. $A = a_0(1+\alpha)\sqrt{\varepsilon}\rho^{-\eta}$ is the strain intensity factor, where $a_0 = (1+\alpha\varepsilon)^{-1} W_0$ and $\alpha \equiv \frac{1-2\eta}{1+2\eta}$, $\varepsilon = \rho/R$. For $n > 0$, η is a monotonically *decreasing positive function* of *n,* with a maximum value of 0.5 at $n = 0$ (no damage) and becoming zero as n approaches infinity (*SI Appendix*, Fig. S3 in *supporting information*). Therefore, Eq. **3** indicate that the strain field is more singular than the elastic solution without damage ($n = 0$ and $\gamma \sim r^{-1/2}$ (12, 24). Specifically, inside the damage zone: When $n \to 0$, we have $a_0 \to W_0$ and $\eta \to \frac{1}{2}$, consistent with usual square root elastic singularity; when $n \to \infty$, the strain field approaches $1/r$ since $\eta \to 0$. Hence damage increases the strain singularity near the crack tip. The key factor controlling the delocalization in MNE is η. For SN, $n \gg 1$ and η is small, whereas for MNE, $n < 1$, i.e., η is large; as a result, the strain singularity near the crack tip in SN is much more severe than in MNE.

The critical strain directly ahead of the crack tip at fracture $\gamma_{\theta f}$ is obtained using Eqs. (2 and **3**) and this results in (see SI for more details)

$$\gamma_{\theta f}(r = d, \theta = 0) = \frac{\gamma_d(1+\alpha)}{\left(1+\alpha\rho_f/R\right)}\left(\frac{G_0}{G_f}\right)^{\frac{0.5-\eta}{n}}, \qquad [5]$$

where $\gamma_d \equiv \frac{W_0}{2\sqrt{Rd}}$ is the strain at $r = d$ for a material without damage. In Eq. (**4**), the key factor is G_0/G_f. Since $0.5 - \eta > 0$, the critical strain $\gamma_{\theta f}$ is found to be much larger in MNE ($n \sim O(1), \gamma_{\theta f} \gg \gamma_d$) than in SN ($n \gg 1, \gamma_{\theta f} \sim \gamma_d$), corresponding to higher fracture toughness.

In summary, the model provides the following insights consistent with the experimental results:

1) The well-documented larger damage zone size (5, 7) (Eq. **2**) and fracture strain (1, 6) (Eq. **4**) in MNE compared to SN (common unfilled elastomers) are consistent with the prediction of the model, due to the partial breaking of the networks (small n).
2) The model allows for a growth of a damage region of size ρ without the propagation of a crack, where the critical size ρ_f at fracture depends on n, i.e., the spatial damage distribution, consistent with the observation (Fig. 1) and ref. 3.
3) A more localized damage (large n) leads to a higher-order singularity in strain field (Eq. **3**), in agreement with our experimental observation by DIC (Fig. 2).

Evolution of Damage During Delayed Fracture

Because the breaking rate of chemical bonds is much faster than typical loading and strain rates achieved under most experimental conditions, the above rate-independent model where damage distribution depends only on the distance from the crack tip describes qualitatively well our observations under *continuous* deformation. However, it has been demonstrated that polymer networks can exhibit time-dependent delayed fracture at *fixed* strain (38–40), even for simple chemical networks (such as PDMS 41) with little viscoelasticity. These fixed strain relaxation experiments strongly suggest that the damage is caused by the slow and progressive breaking of chemical bonds (42). Here, we show that the spatial distribution of the damage governs the delayed fracture behavior of different materials as well, and MNE avoid delayed fracture by redistributing stress in the damage zone.

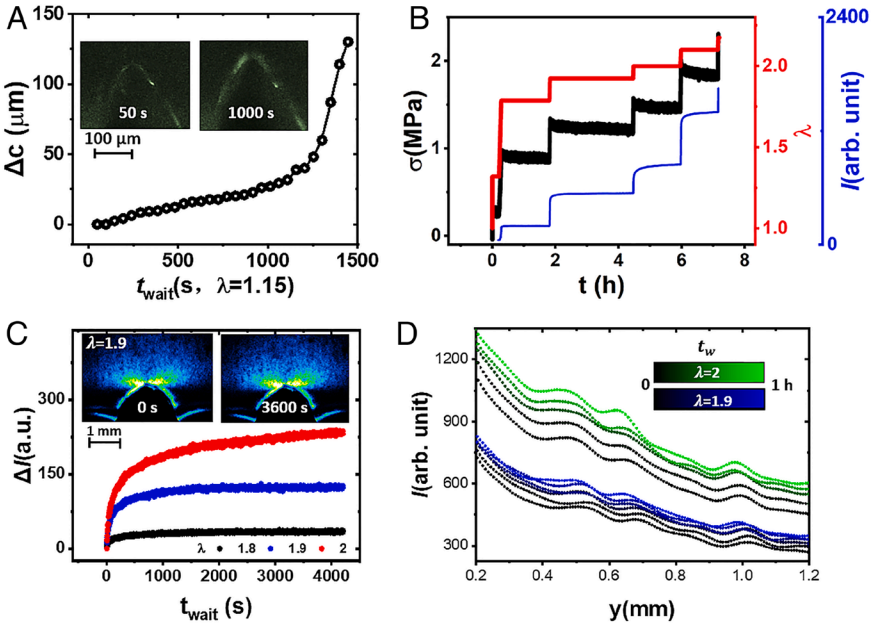

Fig. 4. (*A*) Crack propagation length Δc in SN at $\lambda = 1.15$. *Inset*: fluorescence image around the crack tip at $t_w = 50$ s and 1000 s, respectively. (*B*) Stress (black), stretch (red), and averaged fluorescence intensity I (blue, 0.3 mm from the crack tip) as the function of time for the TN. (*C*) The change of averaged fluorescence intensity ΔI (calculated over a 0.5 mm × 0.5 mm region at 0.3 mm from the crack tip) for TN at different λ. *Inset*: fluorescence image around the crack tip at $t_w = 50$ s and 1000 s, for $\lambda = 1.9$. (*D*) Fluorescence intensity as a function of distance from the crack tip for $\lambda = 1.9$ (blue) and $\lambda = 2$ (green). Each curve corresponds to a different increasing waiting time.

The occurrence of the delayed fracture behavior was investigated in SN and TN (labeled with mechanophores crosslinkers) in fixed grips conditions, by increasing the nominal λ step-by-step and holding the grips fixed for at least 0.5 h after each step. In the SN, delayed crack propagation in these static conditions can be observed at values as low as $\lambda = 1.15$, and the increase in crack length *c* is defined as Δc and is plotted as function of waiting time t_w at that value of λ during the fixed grip relaxation experiment, in Fig. 4*A*. The crack first grows at a speed ċ around 40 nm/s, and gradually accelerates to ċ ~ 300 nm/s after $t_w > 1{,}300$ s, showing self-acceleration. The acceleration of the propagation at fixed λ will lead to final breaking of the material. During this delayed propagation, an increasing fluorescence intensity is observed at the crack tip (inset images in Fig. 4*A*), which is due to the increasing propagation speed, as fluorescence microscopy is collecting the accumulated intensity during the fixed exposure time (4 s).

For the TN, delayed fracture is never observed during the waiting time, repeated in more than 10 tests. Fig. 4*B* shows an example, where five steps of stretching from $\lambda = 1.3, 1.8, 1.9, 2$ to 2.1 were applied with $\dot{\lambda} = 0.002\ s^{-1}$ each followed by a waiting time of the order of an hour. Crack growth and macroscopic failure occurs at $\lambda = 2.17$, during continuous loading conditions. The averaged fluorescence intensity *I* is calculated over a 0.5 mm × 0.5 mm region at 0.3 mm from the crack tip. For all steps with $\lambda \geq 1.8$, *I* increases with time during the waiting time, showing damage accumulation at the crack tip at fixed macroscopic strain (fixed grips), as shown in Fig. 4*C*. 2D damage maps for $\lambda = 1.9$, at $t_w = 0$ s and $t_w = 1$ h are shown in the inset of Fig. 4*C* and visually, damage maps are slightly brighter at $t_w = 1$ h. The slight increase of the fluorescence intensity during the waiting time after the step in deformation was observed in several different samples, as seen in *SI Appendix*, Fig. S5 in *Supporting Information*. The increase of the fluorescence intensity takes place over a large range and over the whole detection area, up to 2 mm from the crack tip, as seen in Fig. 4*D*. Interestingly even though the absolute values of the damage are different for the two applied macroscopic λ, the kinetics of damage accumulation shown in Fig. 4*D* shows a weak dependence on position y. Since each position y corresponds to a different local strain (Fig. 2*B* this result implies that higher values of stretch in these MNE do not cause a higher rate of damage, at least within the range that we can detect here optically. Note that in all experiments we cannot detect a *motion* of the crack tip within our optical resolution of about 2 μm. Hence the damage increases while the crack does not move and the macroscopic stress decreases.

The concomitant accumulation of damage during relaxation and absence of delayed fracture in the TN shows that a different mechanism must be active in this delayed fracture experiment than in SN. In principle delayed fracture can be understood by considering a time-dependent damage model (42), where the kinetics of bond scission is expressed by:

$$b_i = b_{i0}\exp\left\{-\frac{n_i}{\tau}\int_0^t exp\left[3\zeta\frac{\sqrt{I_1(x,y,t')/J_i}}{1-I_1(x,y,t')/J_i}\right]dt'\right\}, \quad [6]$$

b_i and b_{i0} are the density of elastic chains per unit volume of material, at time *t* and in pristine conditions, respectively, in the *i*-th type of chains. τ is the relaxation time for chain dissociation, n_i is the number of monomers per chain. $\zeta \equiv \frac{L_a}{L_k}$, where L_a is the activation length for bond dissociation and L_k is the Kuhn length. I_1 is the strain invariant, a function of time and position. For uniaxial extension, $I_1 = \lambda^2 + \frac{2}{\lambda}$. J_i is a material constant representing chain extensibility and it increases with chain length. More detail can be found in *Supporting Information* and also ref. 42.

According to Eq. **6**, for a known material with fixed $\frac{n_m}{\tau}$ and ζ, bond breaking kinetics depends on $I_1(x,y,t)/J_i$. When $I_1(x,y,t) \to J_i$, breaking kinetics is faster than the time scale of deformation at the applied stretch rate $(1/\dot{\lambda})$, so that massive damage is detected during continuous deformation. Since $I_1(x,y,t)$ is an effective measure of strain magnitude, a higher strain is required to effectively break bonds at a given rate for long chains (large J_i). For SN, both damage and strain distribution are highly localized (large *n* in Eq. **2**), the drop in breaking kinetics along the distance from the crack tip is rapid. Breakage close to the damage zone is rather fast, taking place during deformation, while far away from the crack tip, chains bear only the macroscopic strain, remaining almost intact. To further propagate the crack, the time-dependent damage takes place very close to the crack tip because of the increasing I_1 due to the propagation of the original crack, observable as delayed fracture in SN and also from a high strain rate observable in front of the crack (Fig. 2*A*).

In the MNE, the secondary and tertiary networks can be seen as parallel networks with a much longer average chain length than the primary network and no prestretch, so that their breaking kinetics are much slower than that for the shorter prestretched chains, preventing the crack from propagating. Fracture happens only when most of first network is damaged and the secondary/tertiary networks are effectively fully loaded. However, due to the less concentrated strain distribution, the breaking kinetics of the chains of the first network around the crack tip in MNE is more uniformly distributed. After a large step in strain, the first network far from the crack is already significantly damaged (see Fig. 4*D*), while the time scale to damage the secondary network at the same strain is still relative long, so that no delayed crack growth is detected. Once propagation starts, it appears as a rapid process during deformation, due to the similar damage rate at different distances from the crack tip. A much faster loading rate would be required in the experiments to observe a delayed fracture (probably taking place still over a short time scale after deformation). It is also worth noting that even though the strain level is much higher at larger λ or closer to the crack (see Fig. 2 *B* and *C*, there is not a dramatic increase in damage accumulation rate (Fig. 4*D*). In fact, due to the polydisperse chain length in the filler network (with different maximum values of the extensibility parameter J_i), the same bond breaking kinetics occurs at different values of λ. Shorter chains of the filler network break at lower strain or further away from the tip while longer chains of the same primary network break at higher values of λ, i.e. closer to the crack tip. Finally, the very long and less stretched chains of the secondary network only break beyond the observation time. In essence the breakage revealed by the mechanophores does not significantly overload the second network until the first network is highly damaged and stress transfer occurs(30). This result is consistent with the work done with Spiropyran as a mechanophore showing that the transfer of stress to the secondary network only occurs when the first network is highly damaged.

Conclusion

We showed that the simultaneous mapping of molecular damage and strain field as a function of time provides a valuable tool to describe the mechanisms of initiation of fracture in model tough elastomers based on interpenetrated networks. Unlike previous studies focusing on the steady-state propagation of a crack, our measurement directly targets the transient behavior before or at the onset of crack propagation.

While simple elastic networks follow well the picture of Lake and Thomas with a localized damage at the crack tip systematically leading to crack advance, the MNE, representative of tough elastomers, do not. We clearly observe that TN elastomers form a large molecular damage zone that is much more diffuse around the crack tip. As the load is increased or maintained constant, the molecular damage increases but the stress and strain fields become less singular and do not necessarily lead to crack propagation but to a blunting of the crack. At very high applied stress when the damage is extensive a fast propagation occurs in a highly damaged zone.

Based on these results, we propose a model focusing on the coupling between strain and stress field and damage. The classical discussion on fracture energy Γ considers steady-state propagation: Energy is only dissipated by molecular damage caused by the creation of new surfaces.

Introducing a distribution singularity parameter n, our model captures many features of the coupled damage and deformation observations: A less singular damage results in a reduction of strain concentration and to an increase in fracture strength. This result is consistent with the results of Slootman et al. (16) showing only a qualitative correlation between number of damaged bonds during steady-state crack growth and fracture energy. We propose a fracture criterion determined by a critical level of damage (represented by a critical level of the modulus G_f at a short distance, d, from the crack tip) to cause crack growth. This damage approach avoids reliance on a critical fracture energy, which becomes challenging to define when damage spreads extensively throughout the material, as the fracture process and damage become strongly coupled.

Built around the damage model, we propose a time-dependent damage mechanism to explain the delayed fracture behavior of both SN and TN, where strain and chain length decides the bond breaking kinetics. Experiments in fixed grips conditions show that the polymer chains in the secondary network of the TN introduce a second time scale and prevent the material from fracturing, while a progressive damage accumulation due to the breakage of the more stretched chains of the primary network is observed leading to a progressive blunting of the crack. However, if the strain is increased to a level where the primary network is fully damaged at the crack tip, the less localized strain distribution seen in Fig. 1 leads to a rapid propagation of the crack, so that no delayed fracture is detected.

Although experimental results have been obtained with a specific network architecture, the delocalization of damage should be a general mechanism to mitigate stress and strain concentration and delay the nucleation and growth of a macroscopic crack. While sacrificial bonds do dissipate energy during crack propagation the amount of energy dissipated upon propagation may not be the only or even the determining toughening factor. Resistance to crack nucleation by spatial delocalization of the damage may be just as important and may inspire ideas to toughen materials.

Materials and Methods

Synthesis of Poly (EA) MNE. SNs are synthesized by photo induced free radical polymerization. EA monomer (purchased from TCI Chemicals, VWR, or Sigma-Aldrich) is mixed with crosslinker 1,4-butanediol diacrylate (BDA, 0.5 mol%) and UV initiator 2-hydroxy-2-methylpropiophenone (1.16 mol%). For samples labeled with mechanophores, the DielsAlder adduct mechanophore diacrylate crosslinker synthesized in-house by a previously described method (16) is introduced (0.02 mol%). A customized mold is prepared with a rectangular silicone frame (thickness 1 mm, length 8 cm, and width 5 cm, with injection inlet), constrained between glass plates with PET films between silicone and glass. The mixture is injected into the mold and polymerized under UV (10 $\mu W/cm^2$) for 2 h. After preparation, the elastomer is dried under vacuum and heated at 50 °C overnight. The initial thickness of the SN is around 0.8 mm. DN are prepared by first swelling a SN in 40 g EA monomer, with crosslinker BDA (0.01 mol%), and initiator HMP (0.01 mol%), for 2 h. Then the sample is taken out of the bath, wiped from excess monomer, fixed between two glass plates and polymerized under UV (10 $\mu W/cm^2$), also for 2 h. TN are made in a same way based on DN.

Elastomers are then cut into rectangular samples with length (between the clamps) 15 mm and width 6 mm. Notches are made with razor blades with thickness of 0.1 mm. The ordinary manual cutting (pressing the blades on the surface of the sample) unavoidably creates initial massive activation of mechanophore and the crack profile is very different along the thickness direction, as the elastomer is deformed upon cutting, especially for DN and TN. For an ordinary mechanical testing this effect can be ignored, while it interferes with the 3D damage visualization with micron resolution. To avoid the thickness-dependent damage and crack profile, notches in DN and TN are made by approaching the sample perpendicularly onto a fixed razor with a speed of 0.05 mm/s and holding the blade at a cutting depth of 3 mm, waiting for the razor blade to break through the lateral surface. Even after breaking the surface, due to the friction and deformation, the notch length is not precisely controlled, but with an error within 0.5 mm. In this way, the notch length is around 1.5 mm, with less initial activation of mechanophore and relatively clear cut. The uncertainty due to crack length is tested in different samples, and the strain distribution is not very sensitive to the change in crack length.

Mechanophore Imaging By Confocal Microscopy. A Nikon AZ-100/C2+ confocal microscope was used for the measurement, with the objective AZ Plan Fluor 5× (focal length of 15 mm). In confocal microcopy, depth-resolved images were collected with 14 slices (exposure time 4 s for each slice, depth-step: SN: 117 μm, DN: 130 μm and TN: 154 μm) for each scan, covering the total thickness of the material and one scan cycle is 60 s. The field size is 1.4 × 1.4 mm (objective: 3×) for SN, 2.8 × 2.8 mm (objective: 1.5×) for DN and 4.2 × 4.2 mm (objective: 1×) for TN, with total image size of 2,048 × 2,048 pixels. The wavelength of excitation and emission detection are respectively 405 nm and 450 to 520 nm. With slices in one scan, 3D images can be generated and visualized here with maximum intensity projection to optimize the 3D feature in the image (43).

DIC. The sample surface was prepared by spray painting. The surface was first brushed with white paint and then sprayed with black ink (Molotow Belton Premium Spray Paint). The bottom face of the sample is illuminated with an expanded green laser with a wavelength of 532 nm and images are collected by a CMOS camera (BASLER acA2000-340 km) with pixel size of 0.01 mm/pixel. To avoid the interference of intensity fluctuation from excitation in confocal microscopy, a polarizer, and a filter (only letting in green light) were applied before the camera to block the confocal laser. DIC is processed by the open resource program pyDIC, developed by Damien André (44). Displacement and strain fields can be calculated from the analysis of successive images and added to obtain results in large strain, with a region of interest of 15 × 15 pixels (0.15 mm × 0.15 mm). Results in this work are shown in the reference configuration, except the inset of Fig. 2*B*.

The deformation gradient tensor $\boldsymbol{F}$ is calculated from the displacement field $\boldsymbol{U}$ (45):

$$\boldsymbol{F} = \nabla \boldsymbol{U} + \boldsymbol{I}. \quad [7]$$

Then the Hencky strain tensor $\boldsymbol{\varepsilon}$ is given by

$$\boldsymbol{\varepsilon} = \ln(\boldsymbol{F}\boldsymbol{F}^{\boldsymbol{T}})^2. \quad [8]$$

Strain rate can be calculated with only two successive images taken at a known time interval, which indicates deformation concentration but avoids the cumulative errors during large strain calculation. In Fig. 2*A*, the spatial velocity gradient tensor $\boldsymbol{L}$ is applied instead of $\boldsymbol{\varepsilon}$ to intuitively compare the singularity in different materials. $\boldsymbol{L}$ at a certain waiting time t_{w0} is calculated by $\boldsymbol{\varepsilon}$ from images $t_{w0} - T$ to $t_{w0} + T$ (using image at $t_{w0} - T$ as reference state, $T = 25$ s in Fig. 2*A* and *SI Appendix*, Fig. S5):

$$\boldsymbol{L} = \frac{\boldsymbol{\varepsilon}}{2\boldsymbol{T}}. \quad [9]$$

Data, Materials, and Software Availability. The images and data have been deposited on Zenodo (46).

ACKNOWLEDGMENTS. We thank Rong Long and Xingwei Yang on valuable discussion on strain analysis. LC gratefully acknowledges support from the Institut Universitaire de France. Parts of this manuscript have been adapted from the thesis of Jianzhu Ju, PSL University, (2021). https://pastel.hal.science/tel-03917146. This work was financially supported by The European Union's Horizon 2020 Programme for Research and Innovation under Marie Skłodowska-Curie grant agreement no. 765811 (DoDyNet) ERC Grant agreement AdG no. 695351 (CHEMECH) ANR MultiNet (grant no. ANR-20-CE06-0028-01) NSF under Grant No. CMMI-1903308.

Author affiliations: [a]Sciences et Ingénierie de la Matière Molle, CNRS UMR 7615, École supérieure de physique et de chimie industrielles de la Ville de Paris, Sorbonne Université, Paris Sciences et Lettres Université, Paris 75005, France; [b]McKetta Department of Chemical Engineering, The University of Texas at Austin, Austin, TX 78723; [c]Laboratoire Charles Coulomb (L2C), University of Montpellier, CNRS, Montpellier 34095, France; [d]Institut Universitaire de France, Paris 75005, France; and [e]Sibley School of Mechanical and Aerospace Engineering, Cornell University, Ithaca, NY 14853

1. J. P. Gong, Why are double network hydrogels so tough?. *Soft Matter* **6**, 2583–2590 (2010).
2. E. Ducrot, Y. Chen, M. Bulters, R. P. Sijbesma, C. Creton, Toughening elastomers with sacrificial bonds and watching them break. *Science* **344**, 186–189 (2014).
3. J. Slootman, C. J. Yeh, P. Millereau, J. Comtet, C. Creton, A molecular interpretation of the toughness of multiple network elastomers at high temperature. *Proc. Natl. Acad. Sci. U.S.A.* **119**, e2116127119 (2022).
4. G. E. Sanoja *et al.*, Why is mechanical fatigue different from toughness in elastomers? The role of damage by polymer chain scission. *Sci. Adv.* **7**, eabg9410 (2021).
5. P. Millereau *et al.*, Mechanics of elastomeric molecular composites. *Proc. Natl. Acad. Sci. U.S.A.* **115**, 9110–9115 (2018).
6. T. Matsuda, R. Kawakami, T. Nakajima, Y. Hane, J. P. Gong, Revisiting the origins of the fracture energy of tough double-network hydrogels with quantitative mechanochemical characterization of the damage zone. *Macromolecules* **54**, 10331–10339 (2021).
7. J.-Y. Sun *et al.*, Highly stretchable and tough hydrogels. *Nature* **489**, 133–136 (2012).
8. X. Zhao, Designing toughness and strength for soft materials. *Proc. Natl. Acad. Sci. U.S.A.*, 10.1073/pnas.1710942114 (2017).
9. T. Matsuda, R. Kawakami, R. Namba, T. Nakajima, J. P. Gong, Mechanoresponsive self-growing hydrogels inspired by muscle training. *Science* **363**, 504–508 (2019).
10. C. Chen, H.-F. Fei, J. J. Watkins, A. J. Crosby, Soft double-network polydimethylsiloxane: Fast healing of fracture toughness. *J. Mater. Chem. A* **10**, 11667–11675 (2022).
11. G. J. Lake, A. G. Thomas, The strength of highly elastic materials. *Proc. R. Soc. Lond. series A: Mathematical and Physical Sciences A300*, 108-119 (1967)
12. C. Creton, M. Ciccotti, Fracture and Adhesion of Soft Materials: A review. *Rep. Prog. Phys.* **79**, 046601 (2016).
13. Y. Chen *et al.*, Mechanically induced chemiluminescence from polymers incorporating a 1,2-dioxetane unit in the main chain. *Nat. Chem.* **4**, 559–562 (2012).
14. R. Gostl, R. P. Sijbesma, [small pi]-extended anthracenes as sensitive probes for mechanical stress. *Chem. Sci.* **7**, 370–375 (2016).
15. Y. Chen, G. Mellot, D. van Luijk, C. Creton, R. P. Sijbesma, Mechanochemical tools for polymer materials. *Chem. Soc. Rev.* **50**, 4100–4140 (2021).
16. J. Slootman *et al.*, Quantifying and mapping covalent bond scission during elastomer fracture. *Phys. Rev. X* **10**, 041045 (2020).
17. T. Matsuda, R. Kawakami, T. Nakajima, J. P. Gong, Crack tip field of a double-network gel: Visualization of covalent bond scission through mechanoradical polymerization. *Macromolecules* **53**, 8787–8795 (2020).
18. M. Liu, J. Guo, C. Y. Hui, A. T. Zehnder, Application of digital image correlation (dic) to the measurement of strain concentration of a pva dual-crosslink hydrogel under large deformation. *Exp. Mechanics* **59**, 1021–1032 (2019).
19. Y. Zheng *et al.*, How chain dynamics affects crack initiation in double-network gels. *Proc. Natl. Acad. Sci. U.S.A.* **118**, e2111880118 (2021).
20. Y. Chen, C. J. Yeh, Y. Qi, R. Long, C. Creton, From Force responsive molecules to quantifying and mapping stresses in soft materials. *Sci. Adv.* **6**, eaaz5093 (2020).
21. Y. Wei, J. Ju, C. Creton, T. Narita, Unexpected Fracture behavior of ultrasoft associative hydrogels due to strain-induced crystallization. *ACS Macro Lett.* **12**, 1106–1111 (2023).
22. T. Zhang, S. Lin, H. Yuk, X. Zhao, Predicting fracture energies and crack-tip fields of soft tough materials. *Extreme Mech. Lett.* **4**, 1–8 (2015).
23. R. Long, V. R. Krishnan, C.-Y. Hui, Finite strain analysis of crack tip fields in incompressible hyperelastic solids loaded in plane stress. *J Mech. Phys. Solids* **59**, 672–695 (2011).
24. R. Long, C.-Y. Hui, Crack tip fields in soft elastic solids subjected to large quasi-static deformation – A review. *Extreme Mech. Lett.* **4**, 131–155 (2015).
25. S. Lee, M. Pharr, Sideways and stable crack propagation in a silicone elastomer. *Proc. Natl. Acad. Sci. U.S.A.* **116**, 9251–9256 (2019).
26. C. Y. Hui, A. Jagota, S. J. Bennison, J. D. Londono, Crack blunting and the strength of soft elastic solids. *Proc. R. Soc. Lond. series: A Mathematical and Physical Sciences 403*, 1489–1516 (2003).
27. G. Scetta *et al.*, Self-Organization at the Crack Tip of Fatigue-Resistant Thermoplastic Polyurethane Elastomers. *Macromolecules*, 10.1021/acs.macromol.1c00934 (2021).
28. H. R. Brown, A model of the fracture of double network gels. *Macromolecules* **40**, 3815–3818 (2007).
29. Y. Tanaka, A local damage model for anomalous high toughness of double-network gels. *Europhys. Lett.* **78**, 56005 (2007).
30. Y. Chen, G. Sanoja, C. Creton, Mechanochemistry unveils stress transfer during sacrificial bond fracture of tough multiple network elastomers. *Chem. Sci.* **12**, 11098–11108 (2021).
31. M. Stratigaki *et al.*, Fractography of poly(N-isopropylacrylamide) hydrogel networks crosslinked with mechanofluorophores using confocal laser scanning microscopy. *Polymer Chem.* **11**, 358–366 (2020).
32. X. P. Morelle, G. E. Sanoja, S. Castagnet, C. Creton, 3D fluorescent mapping of invisible molecular damage after cavitation in hydrogen exposed elastomers. *Soft Matter* **17**, 4266–4274 (2021).
33. T.-T. Mai, K. Okuno, K. Tsunoda, K. Urayama, Crack-Tip Strain Field in Supershear Crack of Elastomers. *ACS Macro Lett.* **9**, 762–768 (2020).
34. K. Ohno, 3 - Identification of the fracture process zone in concrete materials by acoustic emission in *Acoustic Emission and Related Non-Destructive Evaluation Techniques in the Fracture Mechanics of Concrete*, M. Ohtsu, Ed. (Woodhead Publishing, Oxford, 2015), 10.1016/B978-1-78242-327-0.00003-9 pp. 41-55.
35. E. K. Tschegg, A contribution to mode III fatigue crack propagation. *Mater. Sci. Eng.* **54**, 127–136 (1982).
36. Y. Zheng *et al.*, *How chain dynamics affects crack initiation in double-network gels.* **118**, e2111880118 (2021).
37. R. Kiyama *et al.*, *Nanoscale TEM imaging of hydrogel network architecture.* **35**, 2208902 (2023).
38. D. Bonn, H. Kellay, M. Prochnow, K. Ben-Djemiaa, J. Meunier, Delayed fracture of an Inhomogeneous Soft Solid. *Science* **280**, 265–267 (1998).
39. X. Wang, W. Hong, Delayed fracture in gels. *Soft Matter* **8**, 8171–8178 (2012).
40. Y. Qi *et al.*, Mapping deformation and dissipation during fracture of soft viscoelastic solid. *J. Mech. Phys. Solids* **186**, 105595 (2024).
41. H. M. van der Kooij *et al.*, Laser speckle strain imaging reveals the origin of delayed fracture in a soft solid. *Sci. Adv.* **4**, eaar1926 (2018).
42. S. R. Lavoie, R. Long, T. Tang, A rate-dependent damage model for elastomers at large strain. *Extreme Mech. Lett.* **8**, 114–124 (2016).
43. L. Mroz, H. Hauser, E. Gröller, Interactive High-Quality Maximum Intensity Projection. *Comput. Graphics Forum* **19**, 341–350 (2000).
44. D. André, pydic, a free python suite for local digital image correlation. https://gitlab.com/damien.andre/pydic (2018). Accessed 30 January 2021.
45. W. Liu, R. Long, Constructing Continuous Strain and Stress Fields From Spatially Discrete Displacement Data in Soft Materials. *J. Appl. Mech.* **83**, 011006-1–011006-15 (2015).
46. C. Creton, Raw data for "Role of molecular damage in crack *initiation* mechanisms of tough elastomers." Zenodo. https://doi.org/10.5281/zenodo.13911662. Deposited 10 October 2024.